OPEN ACCESS

Influence of the Diffusion Media Structure for the Bubble Distribution in Direct Formic Acid Fuel Cells

Journal of The Electrochemical Society, 2020 **167** 134502

Influence of the Diffusion Media Structure for the Bubble Distribution in Direct Formic Acid Fuel Cells

Konosuke Watanabe,[1,*,z] Takuto Araki,[2,] Takuya Tsujiguchi,[3,**] and Gen Inoue[4]**

[1]*Graduate School of Engineering Science, Yokohama National University, Hodogaya-ku, Yokohama 240-8501, Japan*
[2]*Faculty of Engineering, Yokohama National University, Hodogaya-ku, Yokohama 240-8501, Japan*
[3]*Institute of Science and Engineering, Kanazawa University, Kakuma-machi, Kanazawa 920-1192, Japan*
[4]*Department of Chemical Engineering, Kyushu University, Nishi-ku, Fukuoka 819-0395, Japan*

Direct formic acid fuel cells (DFAFCs) have received considerable attention because they can generate a higher power density compared to other direct liquid fuel cells. However, when generated CO_2 bubbles are retained in the anode's porous transport layer (PTL), the performance of the DFAFCs deteriorates. The gas–liquid two-phase flow behavior within a PTL is not clear; therefore, in this work the power-generation characteristics of DFAFCs using two types of PTL, carbon paper and carbon cloth, were investigated. It was found that the maximum current density was approximately 60 mA cm^{-2} higher with the carbon cloth than with the carbon paper. The CO_2 bubble distribution in the anode's PTLs was visualized by X-ray computed tomography and discuss the effects of the bubbles on the power-generation performance of DFAFCs. We found that interstices in a carbon-cloth PTL provided pathways for bubble migration and release to the channel, so that the bubbles did not deteriorate the power output. Bubble accumulation in a carbon-paper PTL led to a drop in power output, confirming that the structure of the PTL and the CO_2 bubbles affect the power-generation characteristics.

 [DOI: 10.1149/1945-7111/abb565]

Manuscript submitted June 13, 2020; revised manuscript received August 22, 2020. Published September 14, 2020. *This was paper 1458 presented at the Atlanta, Georgia, Meeting of the Society, October 13–17, 2019.*

Liquid fuels such as methanol, ethanol, and formic acid, produced using renewable energy, have attracted great attention as energy carriers. There are many advantages of using liquid fuels as energy carriers, including easier transportation and storage compared to hydrogen, high energy density, and the availability of existing infrastructure. A key technology in this concept is the direct liquid fuel cell (DLFC), which converts these liquid fuels directly into electrical energy.[1,2] The direct formic acid fuel cell (DFAFC), which uses formic acid as a fuel, has a higher output compared to other DLFCs; for example, its output is three times higher than that of the direct methanol fuel cell (DMFC) at 303 K.[3,4] In DFAFCs, the chemical reactions which occur are shown in Eqs. 1–3.

$$\text{Anode:}\quad HCOOH \rightarrow CO_2 + 2H^+ + 2e^- \qquad [1]$$

$$\text{Cathode:}\quad 2H^+ + 2e^- + (1/2)O_2 \rightarrow H_2O \qquad [2]$$

$$\text{Overall:}\quad HCOOH + (1/2)O_2 \rightarrow CO_2 + H_2O \qquad [3]$$

Because of these features, applications in a wide range of fields—from power supplies for small portable electronic devices to large emergency power generators—are expected.

There are some issues related to the practical application of these devices, for example, the power output of DFAFCs decreases over time. The decrease in power output can be roughly classified by two reasons; the first is because of catalyst poisoning,[5–8] and the second is an increase in mass-transport resistance by the generation and retention of bubbles.[9–12]

With respect to catalyst poisoning, Zhu et al.[5] measured the change in current density during a short-term endurance test, in which the power generation at 0.5 V was monitored at different formic-acid concentrations. Their results showed that the power decrease over the power-generation time increased with increasing formic-acid concentration, and when 15 M formic acid was used, a power decrease of about 70% occurred after 3.5 h of power generation. Several methods have been reported to reverse catalyst poisoning. Zhu et al.[5] reported that good polarization characteristics after short-term durability tests were obtained by applying a voltage of 1.2 V to the anode for several seconds. Zhou et al.[8] reported that the polarization characteristics after short-term durability tests could be completely restored by flowing pure water through the anode for one hour.

With respect to the increase in mass-transport resistance by the generation and retention of CO_2 bubbles, CO_2 bubble management is more important in DFAFCs as the amount of CO_2 emitted per electron is higher than that in DMFCs, as such devices are often operated at high current densities. However, there are few reports of bubble management in DFAFCs in literature.[9–12] Saeed et al.[12] designed a selective gas permeable anode flow field for DFAFCs for the efficient removal of CO_2. The polarization curves revealed a 10% increase in the power-generation performance. Thus, although previous studies have investigated the gas–liquid distribution in DFAFCs, most of them have focused on the distribution in the channel, whereas, to our knowledge, there are no reports about the distribution in the PTL.

Looking at other energy devices, there are some reports which have investigated the gas–liquid distribution in DMFCs[13–19] and proton exchange membrane electrolyzers.[20] However, most of them focused on the distribution in the channel and the liquid properties in these energy devices are different to DFAFCs. Hartnig et al.[21] visualized CO_2 bubbles inside a carbon-cloth PTL by synchrotron X-ray radiography, showing that CO_2 bubbles accumulated under the bends of the cloth. However, X-ray radiography can only capture 2D transmission images, so it has not been possible to capture the 3D distribution of CO_2 bubbles in the PTL. Some DMFCs models have been developed and analysis of mass transport by numerical simulation was performed.[22–25] However, an experimental approach is also required to reveal the gas–liquid distribution in the PTL.

Visualization of the CO_2 bubble distribution in DFAFCs during power generation is useful for elucidating the detailed power-reduction mechanism and developing a technology to prevent power loss. Therefore, in this study, the power-generation characteristics using two types of anode's PTL, carbon paper and carbon cloth, were measured and the effects of CO_2 bubble distribution on power-generation performance were investigated by visualizing the CO_2 bubble distribution in the anode's PTL of a DFAFC during power generation, using X-ray computed tomography (CT).

*Electrochemical Society Student Member.
**Electrochemical Society Member.
[z]E-mail: watanabe-konosuke-td@ynu.jp

Experimental

Preparation of the membrane electrode assembly (MEA).—NR-212 (DuPont) was used as the polymer electrolyte membrane (PEM). Two different materials, namely, carbon paper (TGP-H-060, Toray Industries, Inc.) and carbon cloth (Cloth A, Etek), were used as the PTL for comparison in the tests. The PTLs were untreated. The properties of each type of PTL are listed in Table I.[10,26,27] Figure 1 shows scanning electron microscopy (SEM) images of each PTL. The porous transport electrode (PTE) was coated onto each PTL with a catalyst layer (CL). Pd/C (30wt%-Pd, ISHIFUKU Metal Industry Co., Ltd.) was used as the anode catalyst and Pt/C (TEC10E50E, TANAKA Kikinzoku Kogyo K.K.) was used as the cathode catalyst. The ionomer loading of the CL was 50 wt%. The PEM and PTE were combined using a hot press machine (AH-2003, AS ONE Corp.) to produce the membrane electrode assembly (MEA). Hot pressing was performed at 140 °C and 1 MPa for 3 min. The reaction area was 1.0 cm × 1.0 cm. The same type of PTL was used for both anode and cathode electrodes. However, to reduce the influence of structural differences in the cathode's PTL, oxygen was supplied to the cathode in this study.

Cell configuration.—Figure 2 shows a schematic diagram of the DFAFC cell used in this study. To visualize the inside of the DFAFC by X-ray CT, graphite (G347B, Tokai Carbon Co., Ltd.) was selected as flow fields and endplates material due to its good X-ray transmissivity. The flow field has a parallel flow structure with a width of 1 mm, a depth of 1 mm, and a rib width of 1 mm. A hard rubber sheet was used as the gasket to line the outer layer of the PTE, to prevent formic acid and oxygen from leaking out of the cell. PTL was compressed to a specified thickness using a hard rubber sheet, the same used for the gasket, whose thickness did not change under the compression load. The gasket thicknesses were selected so that the compression pressures of the diffusion media would be approximately 0.3 MPa as measured by the pressure-measurement film (Prescale LLLW, Fujifilm Corporation). The carbon-paper PTL thickness was 190 μm and the carbon-cloth PTL thickness was 220 μm after compression. Assuming that the compressed thickness of CL is 10 μm, the compressed porosities are approximately 76% and 63% for the carbon-paper PTL and the carbon-cloth PTL, respectively.

Measurement of the power-generation characteristics.—The formic acid that was supplied to the anode was prepared by diluting 90 wt% formic acid (067-00496, Fujifilm Wako Pure Chemical Industries, Ltd.) with pure water. The formic acid was delivered from the tank to the cell using a squeeze pump (7553-70, manufactured by Masterflex), and excess formic acid was returned to the tank and recirculated. The tank capacity was large enough to maintain the concentration of formic acid and the formic acid concentration reduced by only 0.3 wt% after the experiment. Product CO_2 was returned to the tank with the formic acid, where the gas and liquid were separated, and then, the CO_2 was released to the atmosphere. The flow rate of the dry oxygen supplied to the cathode was regulated using a mass-flow controller (PAC-D20 and SEC-N100, HORIBA, Ltd.). The operating pressures of formic acid and oxygen were atmospheric. Table II shows the experimental conditions used in this study.

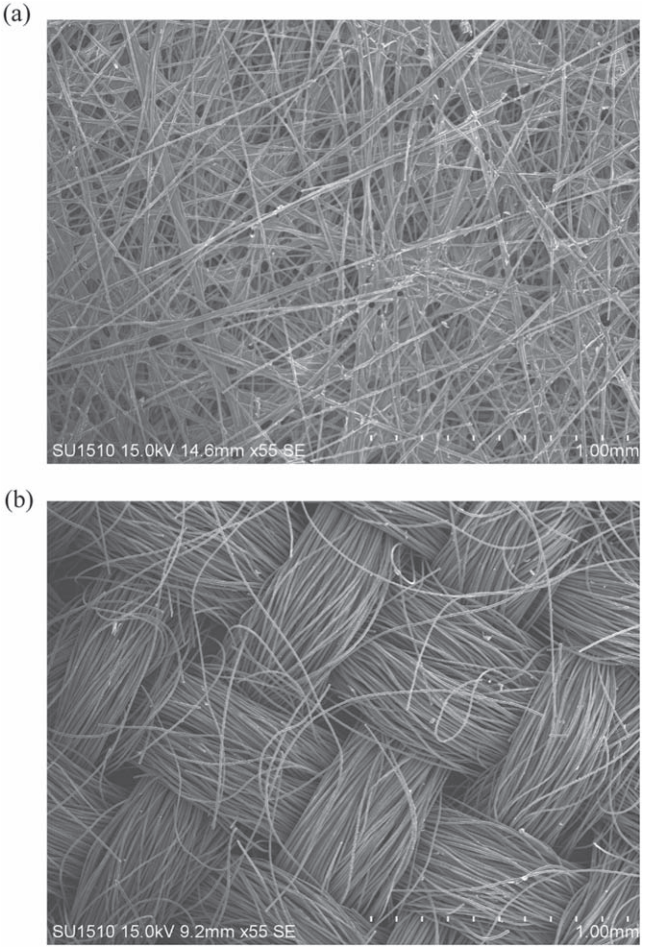

Figure 1. SEM images of the two types of porous transport layer used in this study. (a) Carbon paper. (b) Carbon cloth.

The voltage and the current were controlled during power generation using an electronic load device (PLZ164WA, Kikusui Electronics Corp.) and were measured at a sampling period of 1.0 s using a data logger (MX100, Yokogawa Electric Corp.).

Before the measurements, power was generated by the fuel cell at 0.4 V for one hour as an initial conditioning, and the high-frequency resistance (HFR) was measured using a chemical impedance analyzer (IM3590, Hioki E.E. Corp.). Subsequently, to recover the decrease in power-generation performance caused by catalyst poisoning over time, pure water was delivered to the anode until the cell voltage was 0.1 V or less (recovery process), as described previously by Zhou et al.[8] The power-generation characteristics were measured during a voltage sweep at a sweep rate of -5 mV sec^{-1} from the open circuit voltage to 0 V.

Visualization of CO_2 bubble distribution.—Figure 3 shows the principle of X-ray CT. A three-dimensional X-ray CT system

Table I. Properties of each type of porous transport layer (PTL)[10,26,27]

PTL	TGP-H-060 (Carbon paper)	Cloth A (Carbon cloth)
PTL	TGP-H-060 (Carbon paper)	Cloth A (Carbon cloth)
Thickness (Without catalyst layer)	190 μm	360 μm
Porosity (Uncompressed)	78%	80%
Contact angle (Cassie mode)	130°–140°	130°–140°
Catalyst loading	Anode: 2.0 mg cm^{-2}, Cathode: 2.0mgcm^{-2}	Anode: 1.9 mg cm^{-2}, Cathode: 2.9mgcm^{-2}

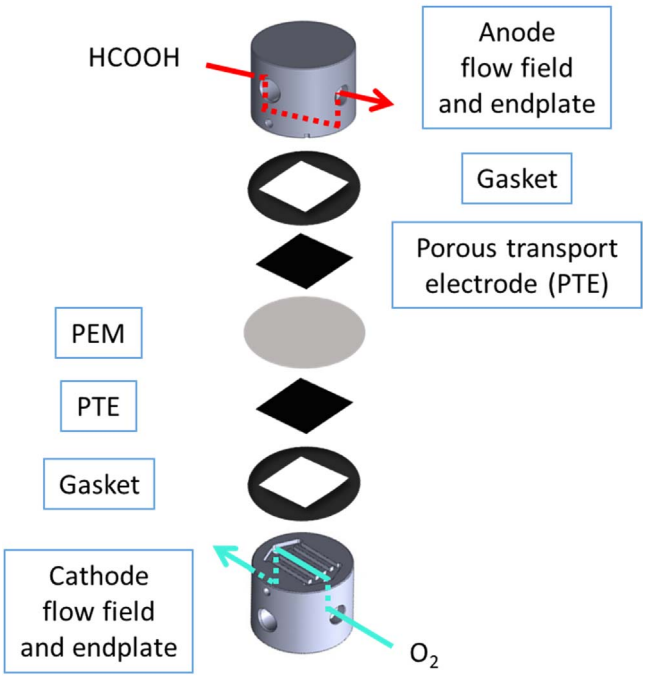

Figure 2. Schematic diagram of the direct formic acid fuel cell.

(TDM-1000H-II (2 K), Yamato Scientific Co., Ltd.) was used to visualize the inside of the cell during DFAFC power generation. Table III shows the visualization conditions.

Following the measurement of the power-generation characteristics, after the "recovery process," visualization was performed while generating power at 0.05 V with voltage control for high-current-density operation. The change in current density during visualization was also measured. Since the power-generation performance decreased over time, it was impossible to maintain high-current-density operation with current control, so power generation was performed with voltage control at a minute voltage. Subsequently, the recovery process was repeated and visualization was carried out while generating power at 10 mA cm^{-2} with current control for low-current-density operation.

The obtained image was processed using the ImageJ software (https://imagej.nih.gov). A Gaussian filter of $\sigma = 2$ was applied to the image to decrease the noise. Also, since the X-ray absorption coefficients of the PTL carbon fiber and formic acid are almost equal, the bubble distributions were extracted from the image by binarization processing. The differences between the X-ray absorption coefficients

Table II. Experimental conditions.

Cell temperature		20 °C (Room temperature)
Formic acid	Concentration	30 wt% (6.5 mol l^{-1})
	Flow rate	45 ml min^{-1}
Oxygen	Relative humidity	0%
	Flow rate	100 ml min^{-1}

Table III. Working conditions for X-ray computed tomography image collection.

Tube voltage	30 kV
Tube current	200 μA
Number of views	1800/180°
Average number of flames	5
Exposure time	100 ms
Whole scan time	18 min
Boxel size	2.7 μm

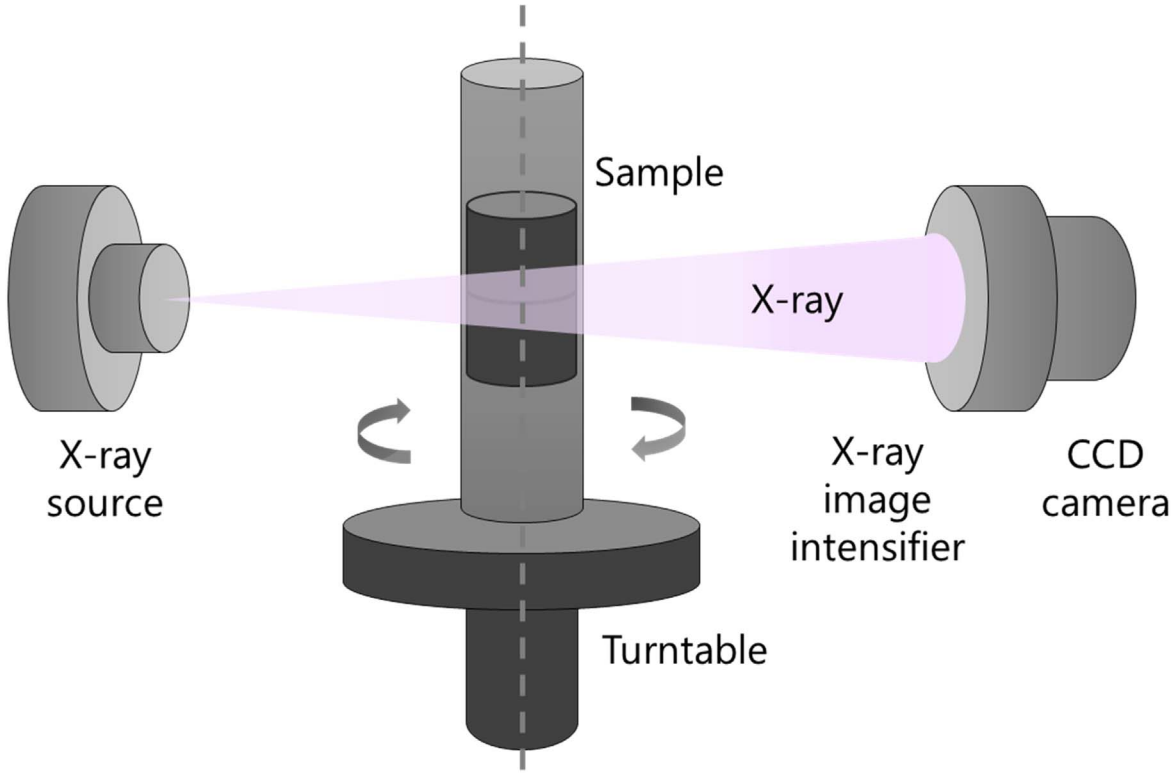

Figure 3. Principle of X-ray computed tomography.

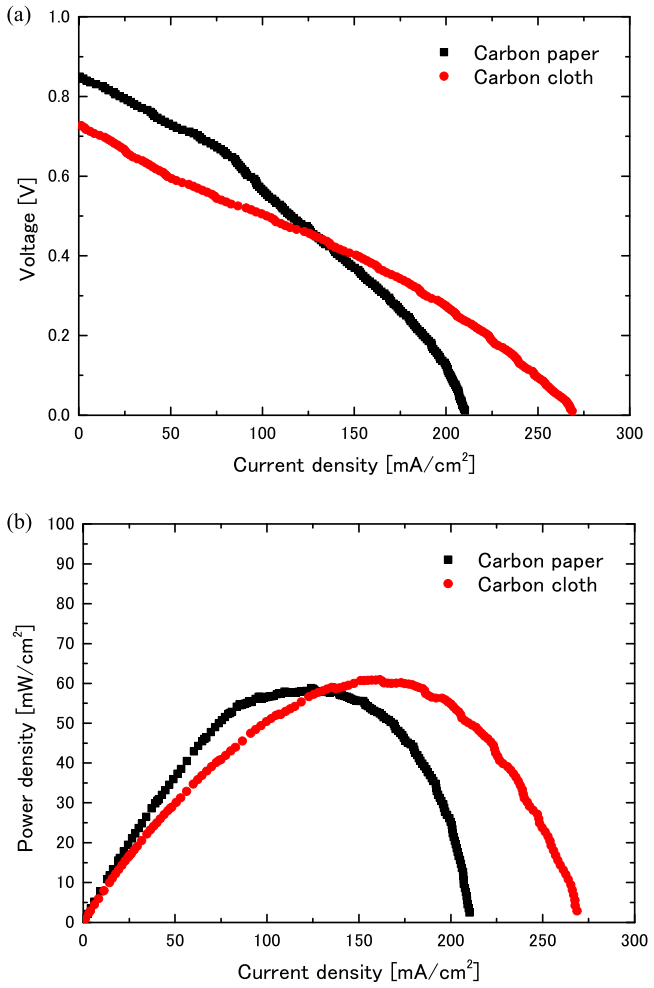

Figure 4. Effect of the porous transport layer structure on the power-generation characteristics. (a) *i–V* characteristics. (b) *i–p* characteristics.

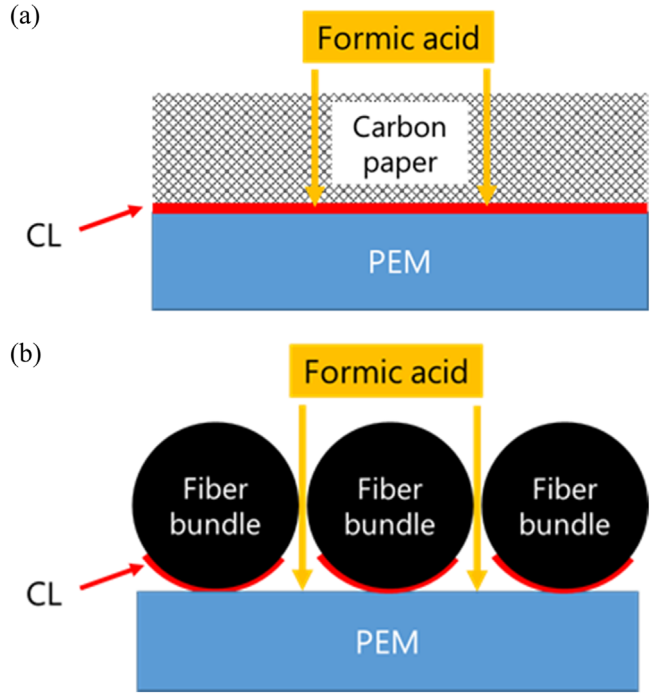

Figure 5. Effect of the porous transport layer structure on a cross over mechanism. (a) Carbon-paper PTL. (b) Carbon-cloth PTL.

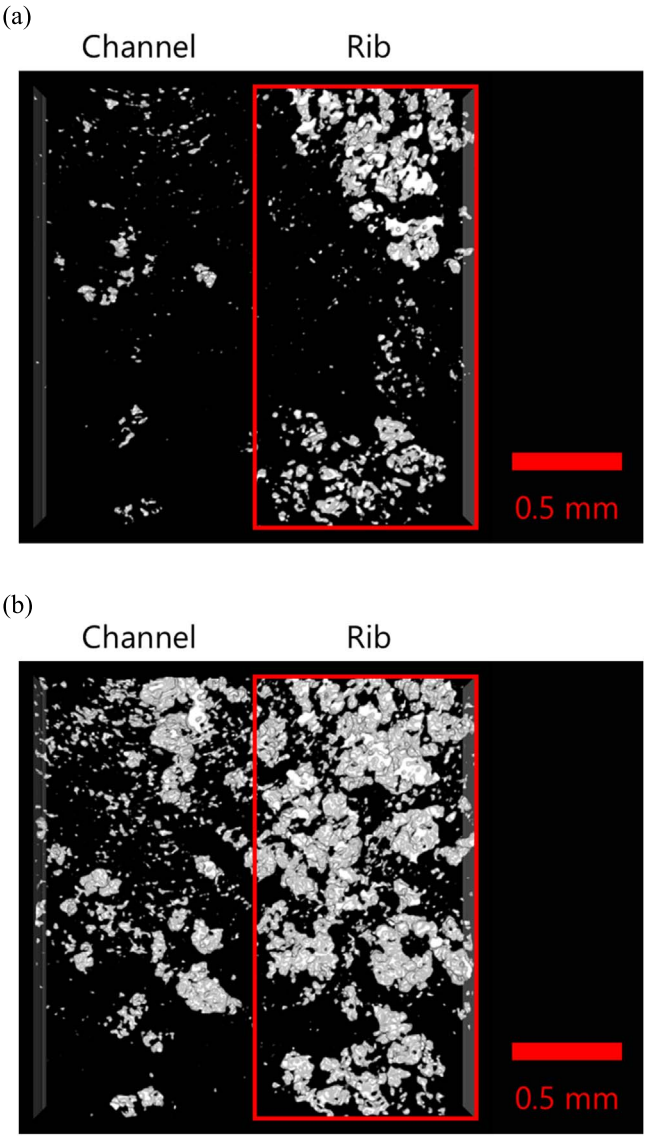

Figure 6. CO_2 bubble distribution for the carbon-paper PTL. The CO_2 bubbles are represented by the irregular white patches in the images. (a) 10 mA cm^{-2}. (b) 139 mA cm^{-2}.

of the channel and the rib of the cathode separator were used to determine the binarization thresholds.

Results and Discussion

Influence of the PTL structure on the power-generation characteristics.—The HFRs measured during the initial conditioning are 190 mΩ and 208 mΩ for the carbon-cloth PTL and the carbon-paper PTL, respectively. It can be seen that both resistances are equivalent.

Figure 4 shows the *i–V* and *i–p* characteristics of the two types of PTL. The open-circuit voltage of the carbon cloth is approximately 0.1 V lower than that of the carbon paper. However, the maximum current density is about 60 mA cm^{-2} higher. The maximum power density of the carbon cloth is approximately 5 mW cm^{-2} higher than that of the carbon paper. The difference in the cross over mechanism between the carbon-paper PTL and the carbon-cloth PTL was considered to cause the initial open-circuit voltage difference. In the carbon-paper PTL (Fig. 5), the CL coated the entire interface, however, in the carbon-cloth PTL, some areas between the carbon fiber bundles remain uncoated by the CL. In the carbon-cloth PTL, a higher proportion of formic acid has direct contact to the PEM in the

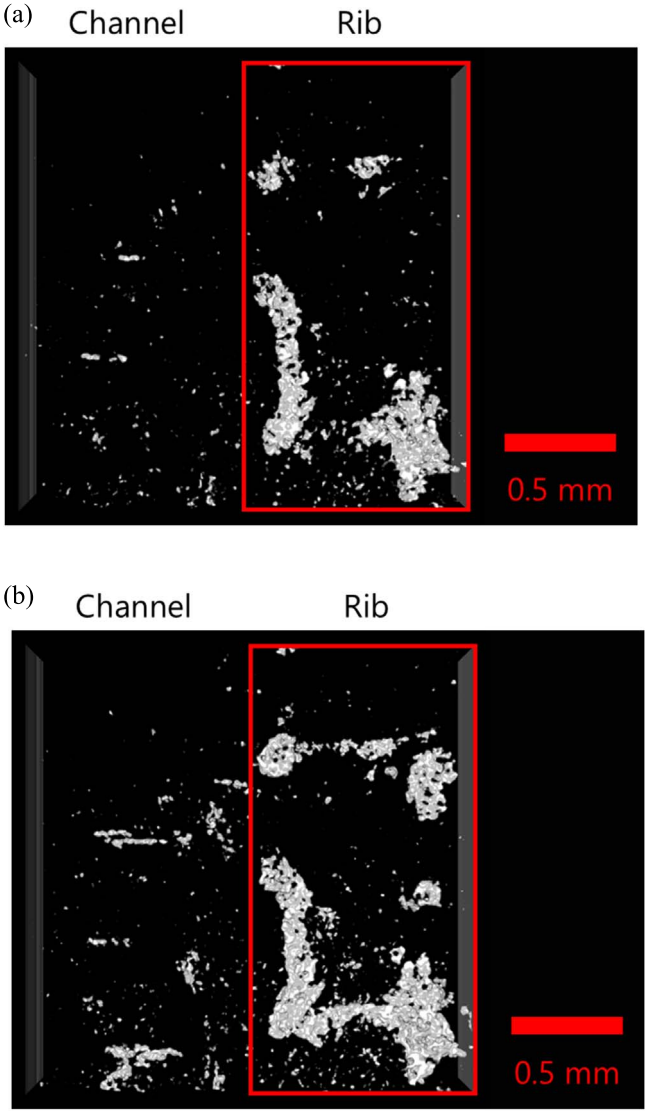

Figure 7. CO_2 bubble distribution for the carbon-cloth PTL. The CO_2 bubbles are represented by the irregular white patches in the images. (a) 10 mA cm^{-2}. (b) 175 mA cm^{-2}.

anode. Therefore, the amount of cross over increased and the initial open-circuit voltage decreased in the carbon-cloth PTL.

In the medium-to-high current-density region of 75 mA cm^{-2} or more, for the carbon-paper PTL, a mass transport loss started from approximately 100 mA cm^{-2}. However, for the carbon-cloth PTL, a mass transport loss did not start until over 200 mA cm^{-2}. As oxygen was supplied to the cathode, a mass transport loss in the cathode could be ignored. Therefore, the difference in the current densities, which the mass transport losses started, depended only on the anode mass transport. In this experiment, it is considered that the difference in the current densities, which the mass transport losses started, is owing to the influence of the CO_2 bubbles in the anode PTL. To investigate the influence of the CO_2 bubbles in the anode PTL, visualization was performed.

Influence of the PTL structure on the CO_2 bubble distribution.—The average current densities while generating power at 0.05 V during visualization are 139 mA cm^{-2} for the carbon-paper PTL and 175 mA cm^{-2} for the carbon-cloth PTL. Figures 6 and 7 shows three-dimensional CO_2 bubble distribution for each anode PTL and two current densities, looking down onto the PTL plane.

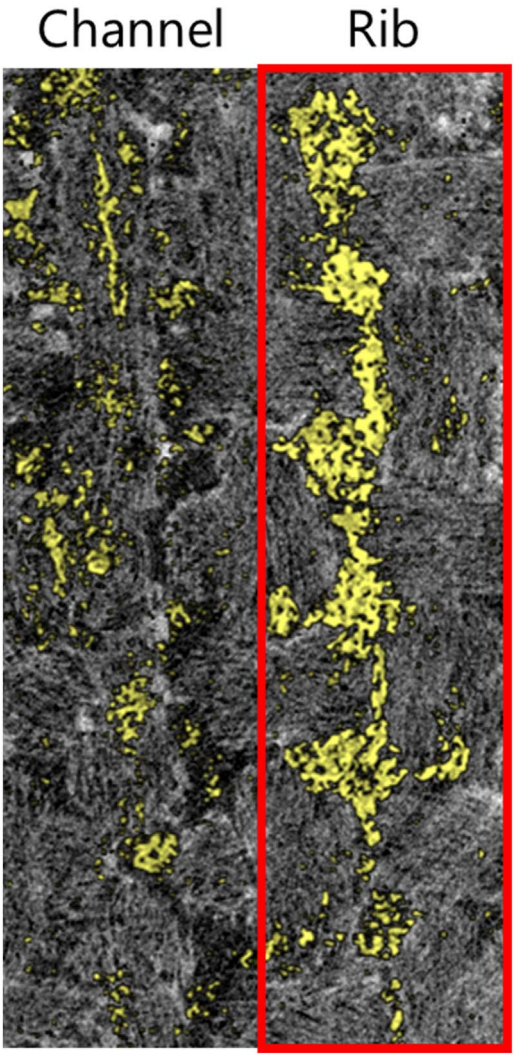

Figure 8. Overlaid image of the bubble distribution on an image of carbon-cloth fibers. The bubbles are shown in yellow and fibers in white.

The CO_2 bubbles are the white parts of the images and the cumulative bubbles through the thickness. More bubbles are present under the rib than under the channel. It is necessary to move once from under the rib to under the channel to discharge. This lengthens the movement distance of the CO_2 bubbles before discharge, which leads to an increase in the transport resistance.

In the carbon-paper PTL, more CO_2 bubbles were observed during high-current-density operation than during low-current-density operation. During low-current-density operation, CO_2 bubbles were only present in approximately 22% of the area under the rib, and almost no CO_2 bubbles were observed under the channel, whereas during high-current-density operation, CO_2 bubbles were found in approximately in 51% of the area under the rib and were widely present under the channel. It is very probable that the power reduction in the carbon-paper measured in the previous section is caused by an inhibition in the supply of formic acid as a consequence of the accumulation of CO_2 bubbles generated at the anode.

When carbon cloth was used for the PTL, no substantial differences were observed between the bubble distributions for low- and high-current-density operation, and the bubbles that were present were partially concentrated. To investigate the concentrated area, the bubble distribution during the high-current-density operation is overlaid on an image of carbon-cloth fibers in Fig. 8. The bubbles are shown in yellow and fibers in white. Figure 8 shows that CO_2 bubbles concentrate at the

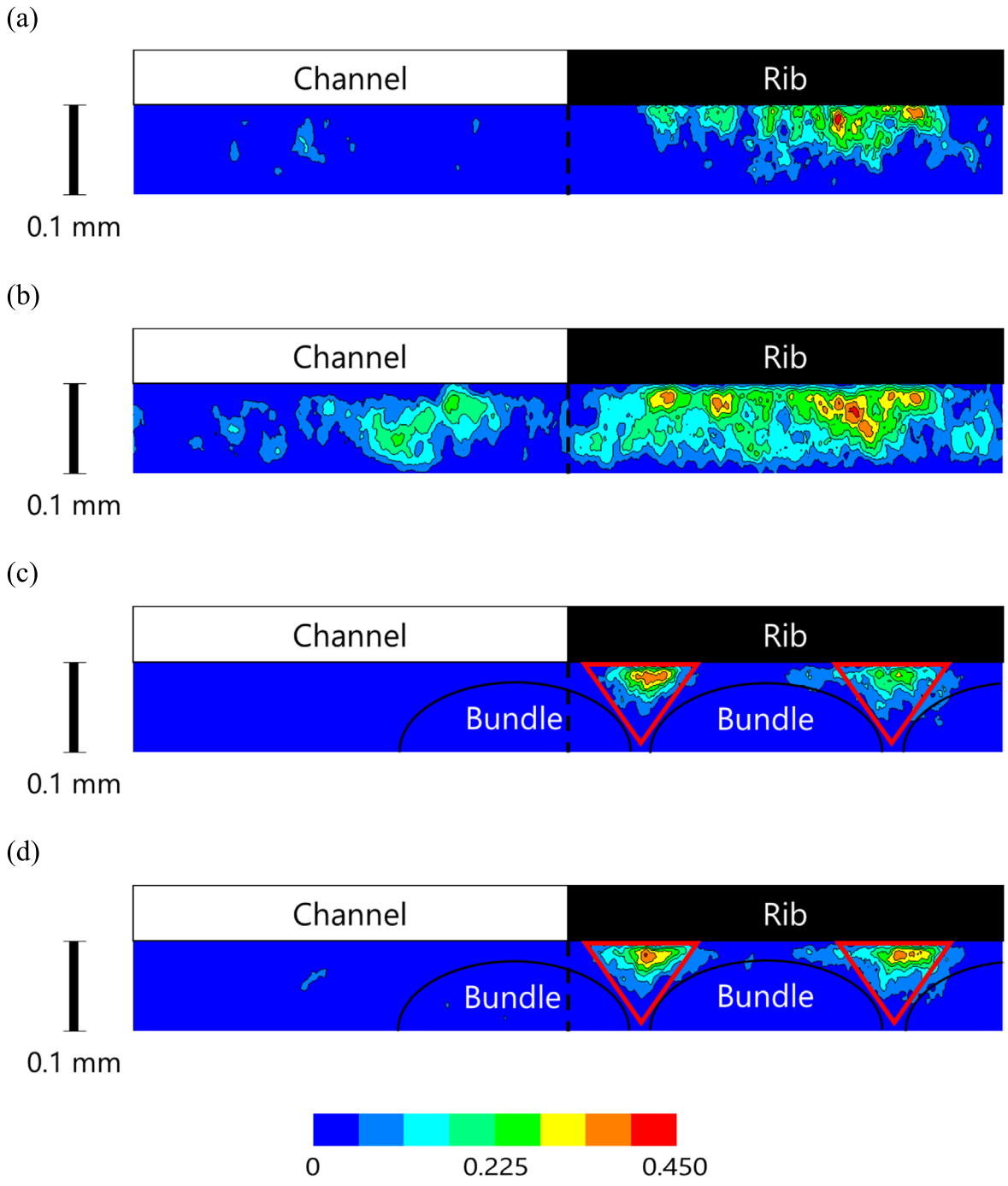

Figure 9. Effect of the porous transport layer structure on the void-fraction distribution. (a) Carbon paper, 10 mA cm^{-2}. (b) Carbon paper, 139 mA cm^{-2}. (c) Carbon cloth, 10 mA cm^{-2}. (d) Carbon cloth, 175 mA cm^{-2}.

intersections of the carbon-cloth bundles and where interstices are generated by weaving. That is, in the carbon cloth, natural pathways are formed between the bundles, which facilitate CO_2-bubble discharge from the CL to the separator and from under the rib to under the channel. It is thought that the output reduction due to mass transport did not occur because the bubbles were efficiently discharged along naturally occurring pathways, and therefore, do not accumulate.

Influence of the PTL structure on the void-fraction distribution.—To quantitatively evaluate the bubble distribution, the normalized average void-fraction distributions in the cross-section perpendicular to the channel directions in each PTL are shown in Fig. 9.

As discussed in the previous section, more CO_2 bubbles were confirmed to be located under the rib than under the channel. In addition, in the carbon-paper PTL, more CO_2 bubbles were formed during high-current-density operation than during low-current-density operation, and CO_2 bubbles were observed under both the rib and the channel during high-current-density operation. In the case of the carbon cloth, only small differences in CO_2 bubble distribution are observed between low- and high-current-density operation, and the CO_2 bubbles are partially concentrated.

In the case of the carbon-paper PTL, CO_2 bubbles were observed in the entire area under the rib during high-current-density operation. At low-current-density operation, the CO_2 bubbles resided in layers

in the middle part of the area under the rib, and no CO_2 bubbles occurred beneath the boundary between the rib and the channel. Since the voids in carbon paper are dispersed, the CO_2 bubbles were also dispersed. Also, during low-current-density operation, no CO_2 bubbles were observed under the channel, so it is likely that the CO_2 bubbles that form under the boundary between the rib and the channel move beneath the channel to be discharged.

In the case of the carbon cloth, the CO_2 bubbles were condensed in the shape of triangles, showed in Figs. 9c, 9d, made by the weaving of carbon fiber bundles during both low- and high-current-density operation. This indicates that the interstices present at the intersections of the carbon-cloth-fiber bundles formed the transport pathways and this pathway leads lower concentration over potential.

Conclusions

The power-generation characteristics of DFAFCs using two different PTL structures were investigated. The maximum current density was about 60 mA cm^{-2} higher in the case of the carbon-cloth PTL compared to carbon paper.

The accumulation of CO_2 bubbles generated at the anode was observed by X-ray CT in operating DFAFCs in PTLs with different structures (i.e., carbon paper and carbon cloth). Interstices present in the carbon-cloth PTL provided pathways for bubble migration and release, meaning that the bubbles did not accumulate so they did not strongly affect the power output over time. Bubble accumulation in a carbon-paper PTL led to a drop in power output, confirming that CO_2 bubbles can affect the power-generation characteristics of DFAFCs.

Acknowledgments

This study was partly supported by JSPS KAKENHI Grant Number 19J20495 and JST PRESTO NW and Mirai. We are grateful to Ryota Mochizuki, Kanazawa University, for preparation of MEA and Dr Kazuya Tajiri, Michigan Technological University, for helpful discussion.

ORCID

Konosuke Watanabe https://orcid.org/0000-0002-1317-3838

References

1. B. C. Ong, S. K. Kamarudin, and S. Basri, *Int. J. Hydrog. Energy*, **42**, 10142 (2017).
2. G. L. Soloveichik, *Beilstein J. Nanotechnol.*, **5**, 1399 (2014).
3. N. M. Aslam, M. S. Masdar, S. K. Kamarudin, and W. R. W. Daud, *APCBEE Procedia*, **3**, 33 (2012).
4. S. Ha, R. Larsen, Y. Zhu, and R. I. Masel, *Fuel Cells*, **4**, 337 (2004).
5. Y. Zhu, Z. Khan, and R. I. Masel, *J. Power Sources*, **139**, 15 (2005).
6. Y. Pan, R. Zhang, and S. L. Blair, *Electrochem. Solid-State Lett.*, **12**, B23 (2009).
7. W. L. Law, A. M. Platt, P. D. C. Wimalaratne, and S. L. Blair, *J. Electrochem. Soc.*, **156**, B553 (2009).
8. Y. Zhou, J. Liu, J. Ye, Z. Zou, J. Ye, J. Gu, T. Yu, and A. Yang, *Electrochim. Acta*, **55**, 5024 (2010).
9. T. Tsujiguchi, F. Matsuoka, Y. Hokari, Y. Osaka, and A. Kodama, *Electrochim. Acta*, **197**, 32 (2016).
10. N. Yamazaki, F. Matsuoka, T. Tsujiguchi, Y. Osaka, and A. Kodama, *FCDIC Fuel Cell Symp. Proc.*, **24**, 239 (2017), (in Japanese).
11. R. Chenitz and J. P. Dodelet, *ECS Trans.*, **16**, 647 (2008).
12. S. Saeed, A. Pistono, J. Cisco, C. S. Burke, J. T. Clement, M. Mench, and C. Rice, *Fuel Cells*, **17**, 48 (2017).
13. Q. Liao, X. Zhu, X. Zheng, and Y. Ding, *J. Power Sources*, **171**, 644 (2007).
14. A. Calabriso, D. Borello, L. Cedola, L. D. Zotto, and S. G. Santori, *Energy Procedia*, **75**, 1996 (2015).
15. W. Yuan, A. Wang, G. Ye, B. Pan, K. Tang, and H. Chen, *Appl. Energy*, **188**, 431 (2017).
16. J. Liang, Y. Luo, S. Zheng, and D. Wang, *J. Power Sources*, **351**, 86 (2017).
17. A. Calabriso, D. Borello, G. P. Romano, L. Cedola, L. D. Zotto, and S. G. Santori, *Appl. Energy*, **185**, 1245 (2017).
18. G. Beckman and W. P. Acker, *Fuel cell membrane and system with integrated gas separation*, WO2002045196A2 (2002).
19. M. S. Defilippis, *Bipolar plate having integrated gas-permeable membrane*, WO2003077342A2 (2003).
20. O. F. Selamet, U. Pasaogullari, D. Spernjak, D. S. Hussey, D. L. Jacobson, and M. D. Mat, *Int. J. Hydrog. Energy*, **38**, 5823 (2013).
21. C. Hartnig, I. Manke, J. Schloesser, P. Krüger, R. Kuhn, H. Riesemeier, K. Wippermann, and J. Banhart, *Electrochem. Commun.*, **11**, 1559 (2009).
22. J. Sun, G. Zhang, T. Guo, K. Jiao, and X. Huang, *Appl. Therm. Eng.*, **132**, 140 (2018).
23. S. L. Ee and E. Birgersson, *J. Electrochem. Soc.*, **158**, B1224 (2011).
24. C. Xu, Y. L. He, T. S. Zhao, R. Chen, and Q. Ye, *J. Electrochem. Soc.*, **153**, A1358 (2006).
25. S. Jung, Y. Leng, and C. Y. Wang, *Electrochim. Acta*, **134**, 35 (2014).
26. J. T. Gostick, M. W. Fowler, M. D. Pritzker, M. A. Ioannidis, and L. M. Behra, *J. Power Sources*, **162**, 228 (2006).
27. S. Simaafrookhteh, M. Shakeri, M. Baniassadi, and A. Alizadeh Sahraei, "Microstructure Reconstruction and Characterization of the Porous GDLs for PEMFC Based on Fibers Orientation Distribution." *Fuel Cells*, **18**, 160–72 (2018).